Wachsmuth-Melm *et al. BMC Methods* (2026) 3:5
https://doi.org/10.1186/s44330-026-00056-9

BMC Methods

METHODOLOGY **Open Access**

On-lamella dual-axis cryo-electron tomography and modelling of lamella stability

Moritz Wachsmuth-Melm[1,2†], Cornelis Mense[2,3†], Santiago Gomez Melo[2,3], Liv Zimmermann[1,2], Ulrich S. Schwarz[2,3*] and Petr Chlanda[1,2*]

Abstract

Background Cryogenic electron tomography (cryo-ET) of cryogenic focused ion beam (cryo-FIB)–milled lamellae enables visualization of three-dimensional cellular architecture in near-native conditions at nanometer-scale resolution. However, cryo-FIB milling is typically performed using rectangular patterns that limit the accessible tilt range, precluding dual-axis tomography. In addition, cryo-lamellae must remain mechanically connected to the cell body and are prone to fracture during preparation and transfer to the cryo-transmission electron microscope (cryo-TEM), reducing experimental throughput.

Methods We developed a cryo-FIB trapezoid milling strategy that permits dual-axis cryo-ET by enabling grid loading with the tilt axis oriented perpendicular to the milling direction. Dual-axis and single-axis cryo-ET datasets were acquired and compared, including single-axis tomograms processed with deep learning–based missing wedge restoration. To address lamella stability, we performed finite element–based mechanical simulations to calculate the build-up of von Mises stresses within different lamella geometries and milling designs.

Results Dual-axis cryo-ET provided additional three-dimensional information compared to conventional single-axis tomography and to single-axis tomograms after deep learning–based missing wedge restoration. This resulted in improved tomogram interpretability and segmentation quality. Furthermore, the mechanical simulations identified stress accumulation and fracture-prone regions within cryo-lamellae, allowing the rational design of milling patterns with enhanced mechanical stability.

Conclusions The trapezoid cryo-FIB milling strategy enables routine dual-axis cryo-ET of cellular lamellae, improving 3D information content and segmentation quality. In addition, the finite element–based mechanical framework provides a predictive tool for optimizing lamella design and stability. Together, these methods increase cryo-ET data quality and throughput and offer valuable training datasets for the further development of deep learning–based restoration approaches.

[†] Moritz Wachsmuth-Melm and Cornelis Mense contributed equally to this work.

*Correspondence:
Ulrich S. Schwarz
ulrich.schwarz@bioquant.uni-heidelberg.de
Petr Chlanda
petr.chlanda@bioquant.uni-heidelberg.de

Full list of author information is available at the end of the article

Keywords Cryo-focused ion beam milling, Cryo-electron tomography, Denoising, Missing wedge information, von Mises stress, Linear elasticity and finite elements simulations

Introduction

Cryogenic focused ion beam (cryo-FIB) milling is the method of choice for producing electron-transparent lamella of vitrified biological samples, which can be studied by cryogenic electron tomography (cryo-ET) [1–4]. Cryo-ET consists of a tilt series acquisition with a defined increment of angle range, typically performed in a dose-symmetric fashion along one tilt axis. Because the lamella has a slab geometry, tilting is typically limited to ± 60°, which leads to missing wedge information in Fourier space. Due to this limitation, tomograms have an anisotropic resolution, and features along the Z-axis are elongated [5, 6]. Several approaches, including deep-learning missing wedge restoration algorithms, have been developed to fill in the missing wedge information in Fourier space [7–10]. However, these methods have not been evaluated using on-lamella dual-axis cryo-ET. In addition, in silico restoration of detailed 3D information can be challenging due to the high density and complexity of biological structures in the cell.

Here, we explore the potential of implementing a dual-axis setup for lamellae prepared by cryo-FIB milling. Dual-axis transmission and scanning transmission electron tomography have been applied before to room temperature samples as well as to vitreous samples [11–14]. To enable grid rotation without unloading the sample, dual-axis stages and holders have been developed and can be integrated into modern TEM systems such as the Titan Krios (Thermo Fisher Scientific) and CRYOARM (JEOL). Krios single-axis holders are marginally more stable during tilting compared to dual-axis holders [15, 16] and are currently installed by default unless a dual-axis holder is requested. Krios dual-axis holders have significantly larger specimen shifts occurring reproducibly upon change of tilt direction during dose-symmetric tilt scheme. This is attributed to the more complex holder geometry and independent moving parts of dual-axis designs. However, in current dose-symmetric acquisition schemes, this effect is effectively minimized by using backlash during tilting – an approach to all tilt angles from the same direction [17].

Dual-axis ET partially complements missing wedge information and can be useful for interpreting complex membranous structures in 3D and improving segmentation accuracy [11]. Cryo-FIB milling approaches currently use rectangular patterns, which lead to a milled lamella attached to perpendicular walls of non-milled remnants of the cell body. The currently used milling geometry enables single-axis tilt series acquisition when the tilt axis is oriented perpendicular to the milling direction. However, it limits or prevents the use of dual-axis tomography, whose application remains to be explored and could augment 3D data quality of cellular material when subtomogram averaging is not applicable. In addition, lamellae produced using rectangular patterns must be loaded onto the microscope stage with an orientation perpendicular to the tilt axis [1]. To ensure correct alignment, the AutoGrid rim is marked to indicate the grid orientation during loading into Autoloader systems (Thermo Fisher Scientific), which can be technically challenging.

The throughput of cryo-FIB milling is steadily increasing due to the increasing use of automation. Several automated software solutions allow coarse milling and the last milling steps to some extent, yielding a final desirable thickness between 150 and 200 nm [18, 19]. During milling, lamella can undergo undesirable deformation or tilting. This is caused mainly by compression in the supporting film and compression forces released during milling. The supporting film, typically made of thin amorphous carbon or silicon dioxide, does not compress as much as gold metal, leading to reduced flatness of the film, so-called crinkling [20]. Lamella tilting or deformations often limit the final milling step, hence producing thicker lamella or lamella with inhomogeneous thickness. Typically, stress relief cuts (also termed micro-expansion joints) are placed in the cell body to release lateral forces applied perpendicular to the milling direction on the lamella, thereby preventing lamella tilting or deformations [21]. However, the physics of lamella geometry as well as stress points of lamella remain to be studied to inform on better milling geometries and to design patterns which would increase lamella stability and therefore throughput.

Here we show that a trapezoid milling pattern allows one to perform dual-axis cryo-ET on lamellae with commercially available microscopes. Dual-axis tomograms have increased 3D information compared to single-axis tomograms, which facilitates automated segmentation and can serve as improved training data for deep-learning missing wedge restoration approaches. Additionally, this study provides insights into physical forces and stress distribution in lamella and makes suggestions for improvement in milling design. We identify the points of fracture onset with the aid of linear elasticity and finite elements simulations, which we mitigate through refining the geometry of the lamella. We show that the point most at risk of fracture is at the connection joint between the lamella and the cell body, and that rounded edges might reduce this risk. However, with too much material at the joints between lamella and cell body, such as too large radii of rounded edges or distance between stress relief cuts and cell body, it becomes detrimental again.

Materials and methods

Plunge freezing of cells

VeroE6 cells were seeded onto Quantifoil SiO_2 R1.2/20 200 Au mesh grids in a 35 mm cell culture dish coated with SYLGARD™ 184 silicone elastomer. Both grids and dishes were glow-discharged and disinfected with 70% ethanol prior to cell seeding. One day after seeding, grids were removed from the medium and directly transferred to a Leica GP2 plunge freezer set to 80% chamber humidity and 37 °C chamber temperature. A 2 µl drop of medium from the cell culture dish was added on the top side of the grid. Grids were blotted for 3.5 s and plunge frozen in liquid ethane at -185 °C.

Cryo-FIB milling of adherent cells

Grids were clipped into ThermoFisher CryoFIB AutoGrids and loaded into an Aquilos 2 cryo-FIBSEM. Target cells were selected in MAPS. After the eucentricity adjustment, lamellae were coated with organometallic platinum and milled manually using trapezoid milling patterns. Cryo-FIB milling currents were determined by beam-limiting customized 15-hole aperture strip provided by Thermo Fischer Scientific with 3 × 10, 2 × 30, 2 × 50, 100, 300, 500, 1000, 3000, 7000, 15,000, 65,000 pA. FIB aperture alignments were performed every other week. The following currents were used: 0.5-1 nA (step 1), 300 pA (step 2), 100 pA (step 3), 50 pA (step 4), 30 pA (step 5 (polishing)).

Dual-axis cryo-electron tomography on-lamella acquisition

Cryo-ET was performed using a Titan Krios Transmission Electron Microscope (TEM, ThermoFisher Scientific) operated at 300 keV and equipped with a Bio-Quantum® LS energy filter with a slit width of 15 eV and K3 direct electron detector (Gatan) using SerialEM [22]. Montaged maps were acquired at 8700× magnification with pixel size 10.68 Å/pixel and approximate defocus of -80 µm. Dual-axis tomography was performed using a dual-axis stage at the Krios G1 that supports rotation of approximately 90°. A and B single-axis tilt series were acquired at 33,000× magnification with a pixel size of 2.589 Å/pixel at -4 µm defocus, with an electron dose of approximately 1.5 $e^-/Å^2$ per projection. A dose symmetric acquisition scheme was used with an A-axis tilt range of + 68° to -52°, start at 8° and B-axis tilt-range + 60° to -60°, start at 0° in 3° increments [17]. Tilt series were acquired in parallel with PACE tomo [23]. Projection images were acquired as movies and motion correction and summing on-fly using was done using the SerialEM SEMCCD plugin.

Dual-axis tomogram reconstruction

Tilt series were aligned using patch tracking (680, 680; seven patches in x and five patches in y direction) and reconstruction was performed using a weighted back-projection algorithm with SIRT-like filter 5 in IMOD [24]. Contrast transfer function correction in 2D and dose-weight filtering was performed in IMOD prior to tomogram reconstruction. Two tomograms were combined in IMOD using overlapping patches (400 × 400 × 200 pixels). Tomograms were binned 3× for figure production.

Finite element simulation

The finite element simulations solve the linear elasticity equilibrium equations with the aid of the open software framework Dolfinx. The vitrified cell is modelled as an isotropic elastic material with a Young's modulus of 8 GPa and a Poisson's ratio of 0.15 [16, 17].

The cell experiences a thermal hydrostatic strain $\epsilon_T = \alpha_c \Delta T I$ with thermal expansion coefficient $\alpha_c = 2 \times 10^{-5} K^{-1}$ and temperature difference $\Delta T = -200K$, where I is the identity matrix. In addition, the bottom surfaces in contact with the substrate have a prescribed displacement of $\vec{u} = \alpha_s \Delta T \vec{x}$, which represents the thermal contraction of the amorphous carbon substrate with thermal expansion coefficient $\alpha_s = 0.79 \times 10^{-5} K^{-1}$ and undeformed position $\vec{x}$. The equations to solve for a displacement field u are thus

$$\nabla \cdot (\sigma(\epsilon(u)) - \sigma(\epsilon_T)) = 0,$$

$$\sigma = \lambda Tr(\epsilon) I + 2\mu \epsilon,$$

$$\epsilon = \frac{1}{2}\left(\nabla u + \nabla u^T\right)$$

After solving for the displacement field, the von Mises stress is computed as $\sigma_{vM} = \sqrt{(3/2)s : s}$, with s being the traceless stress tensor $s = \sigma - Tr(\sigma) I/3$. Here ":" denotes the Frobenius inner product.

Peak stresses, used for joints of increasing curvature radius, were calculated by first isolating elements at the surface of the joint. After which the average of the 98th percentile was calculated, because taking the highest value would have likely been akin to measuring the error of the simulation.

Geometry

The geometry of the meshes was modelled to closely resemble those of the milled cells, orthogonal and Y junction, using version 4.13.1 of Gmsh. For the orthogonal milling pattern, the two cell bodies were modelled to a convex shape by displacing the outer corners of rectangular prisms. Both bodies were based on a prism with dimensions 9.5 µm × 30 µm × 12 µm, with the corners furthest from the lamella displaced inwards by (0, 10, 0) µm for the lower two and (3, 8, -4) µm for the upper two. Both bodies were given an expansion joint 0.5 µm from the lamella of dimensions 0.5 µm × 30 µm ×5 µm, with rounded edges of curvature 0.1 µm. We modelled the lamella itself with a rectangular prism of dimensions 12 µm × 30 µm × 0.2 µm, attached to the bodies at a height of 6 µm. Whenever rounded joints were used, the surface of the joint was parameterised by a one quarter of a cylinder, with the y axis as its horizontal direction. The radius of the cylinder was varied and the cylinder's centre was set to (r, 0, r) µm from the corner of the joint, to create a tangent line with both the cell body and lamella.

The Y junction milling pattern was imitated by modelling the cell bodies as irregular prisms, with eight corners set at Cartesian coordinates (16.5, ± 1.5, 0), (9.7, ± 1.5, 0), (6, ± 1.5, 4), and (9.7, ± 1.5, 8) µm for the right body and the left body mirrored in the yz plane. The expansion joints were again of dimensions 0.5 µm × 30 µm ×5 µm, with rounded edges of curvature 0.1 µm, and placed at distances (15.4, 0, 1) µm from the edge of the lamella. We modelled the lamella itself as a rectangular prism, with the same dimensions 12 µm × 30 µm × 0.2 µm but attached to the bodies at a height of 4 µm.

The meshing was conducted at a base resolution of 0.5 µm for the cell body, with a finer resolution field of 0.066 µm around the lamella. A gradual transition between these fields was applied over a distance of 5 µm in all directions. The total number of meshed elements was in the range of 2^6 elements.

Results

After plunge-freezing VeroE6 adherent cells, EM grids were clipped into FIB-Autogrids (Thermo Fischer Scientific) and loaded into an Aquilos 2 Cryo-FIB-SEM. Mapping and eucentric position of lamella sites were performed in MAPS. With commonly used rectangular milling patterns, parts of the lamella would be inaccessible to tomography because they would be obscured by the surrounding cell body at high tilt angles. The obscured area depends on the surrounding cell height and the milling angle and is given by tan(angle) multiplied by height. Therefore, we used polygonal milling patterns available in the XTUI software of Aquilos 2 cryo-FIB-SEM to create a trapezoid pattern and micromachine a lamella shape compatible with dual-axis tomography. Two isosceles trapezoid patterns were placed so that their shorter bases were facing each other (Fig. 1A). We used a trapezoid geometry as the first milling pattern with an angle of 150°, allowing for ± 60° angle tilting in the direction parallel to the FIB milling. Isosceles trapezoids have two parallel bases (b_1 and b_2) separated by a height (h) and two legs with supplementary congruent angles (150° and 30°), resulting in 180° at each side. To achieve a 60° tilt, the angle at the shorter base must be 150°, and the length of b_1 and b_2 can be calculated based on equation:

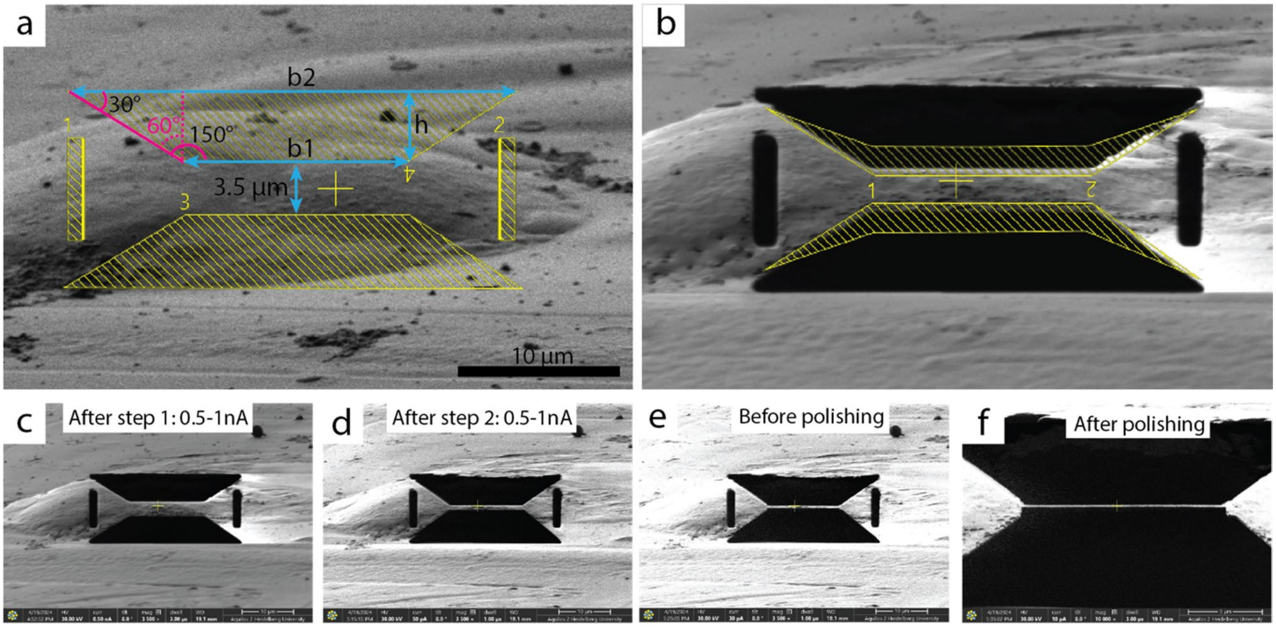

Fig. 1 Trapezoid cryo-FIB milling. **a-f**) Cryo-FIB images of different milling steps. **a**) Two isosceles trapezoids (filled with diagonal yellow stripes and indicated by numbers 3 and 4 are used as a step 1 milling pattern. Isosceles trapezoid bases b1, b2, height h and angles are defined. Patterns 1 and 2 represent stress-release cuts. **b**) Polygonal milling patterns 1 and 2 are used as a step 2 milling pattern. **c-f**) FIB images after step 1, step 2, before and after the polishing step

$$b_2 = b_1 + 2\,h\,cot\,(30^\circ\,)\,.$$

For practical use, b_2 should have double the length of b_1 and h needs to be approximately 4 µm to obtain an angle of 150° at the lower base. We used a trapezoid pattern with b_1 = 14 µm and b_2 approximately 30 µm and h = 4.7 µm. In addition, two rectangular patterns were used for stress-release cuts (micro-expansion joints) [10]. The second polygonal pattern had six vertices to reduce the milling area (Fig. 1B). Subsequent lamella thinning including the last polishing step was performed in 3 steps using rectangular patterns (Fig. 1C-F). All milling steps were performed at a grazing angle of 8–10° and no over-titling was used. SEM was used to monitor each milling step (Fig. 2).

FIB-Autogrids were loaded into a cassette such that the cut-off was facing to the right, and the loading position was verified using a long-distance stereomicroscope. We used SerialEM to acquire medium magnification maps for each lamella at tilt angles 8°, + 68° and − 52° at stage rotation angle 0° and tilt angles 0°, + 60° and − 60°. The nominal rotation between the tilting axes of the two tomograms was approximately 87°. Our data show that the trapezoid milling patterns prevent the cell body from obscuring parts of the lamella at extreme angles, enabling dual-axis tomography on around 80% of the lamella area (Fig. 3).

Tilt series were acquired using SerialEM [22] and in parallel mode using PACE tomo [23]. A-axis was acquired using a dose-symmetric schema and a starting angle of 8°. Subsequently, the stage was rotated by 90°, and B-axis tilt series were acquired. Tomogram positions for the B-axis were manually selected in the PACE tomo routine. Tomograms were reconstructed and combined in Etomo (IMOD version 5.1.0) [24]. Using large patches for combining dual-axis tomograms yielded lower errors, consistent with our previous study [14]. We hypothesized that the reduced exposure dose would decrease the quality of tilt-series alignment. To test this, we did a pairwise comparison of alignment errors between full-dose and half-dose tilt-series, the latter produced by using the -SplitSum flag in MotionCor2. However, we did not find a significant increase in residual error according to a two-sided paired T-test (p = 0.166), showing that tilt series alignment is robust even at half of the total dose typically applied for single-axis cryo-ET. Data and unsupervised segmentations performed in MemBrain [25] clearly showed increased information in the z-direction and improved interpretability of the cellular structures (Fig. 4).

We further aimed to compare the data quality between dual-axis tomography and the deep-learning-based missing wedge correction methods IsoNet [7] and DeepDeWedge [10] trained on single-axis data. Our data show that these methods are unable to fully restore features perpendicular to the tilt-axis present in dual-axis data (Fig. 5). Coupling dual-axis tomography with missing wedge correction by correcting the single-axis tomograms before combination in Etomo improved the data quality mostly along the Z-axis.

Exploring different milling strategies prompted us to evaluate the structural stability of lamella, which was done with the aid of linear elasticity theory and the finite element method (FEM). The vitrified cell was modelled as a linear elastic material with a Young’s modulus of 8 GPa and a Poisson’s ratio of 0.15 [26, 27]. Following standard procedures for material behaviour during temperature changes [28], the sample was subjected to an active strain due to thermal contraction and an additional contractive displacement at the interface with the support

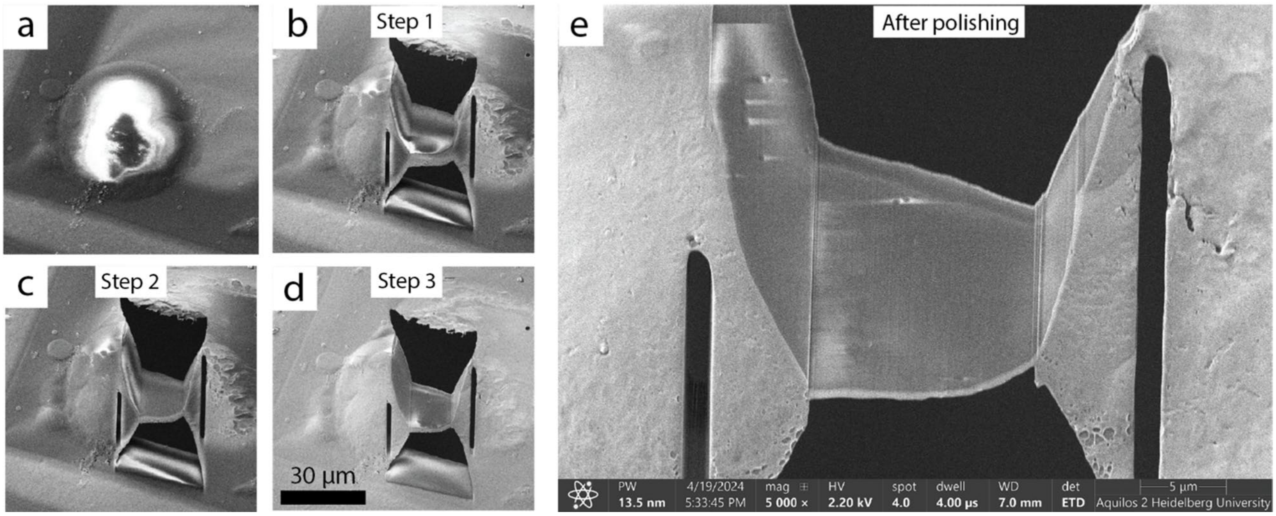

Fig. 2 SEM images of trapezoid cryo-FIB milling. **a-e**) SEM images of different milling steps

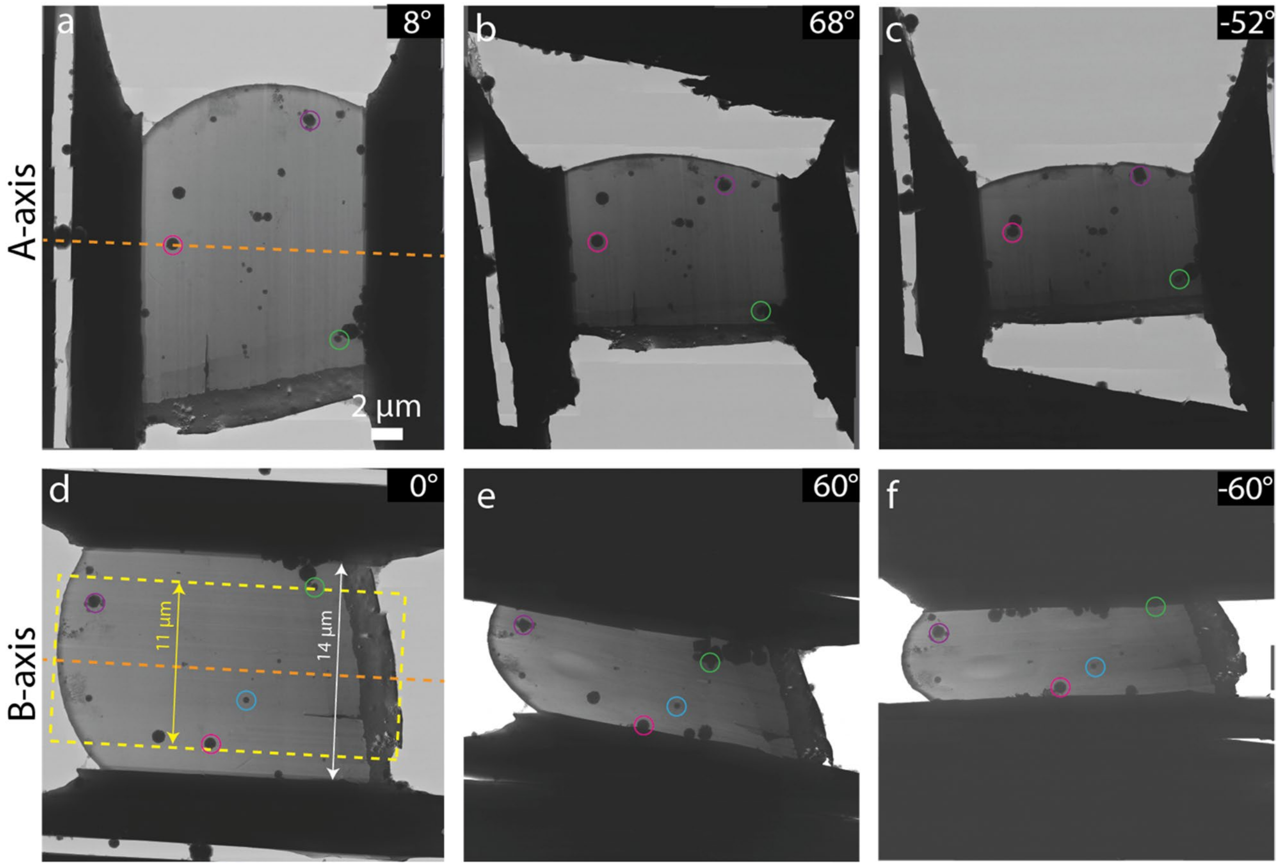

Fig. 3 Cryo-TEM assessment of the dual-axis tilting range with a trapezoid milled cryo-lamella. **a-f**) Cryo-TEM maps were acquired at A- and B-axes and at indicated angles. Ice contamination highlighted by coloured circles was used as fiducial markers to assess lamella electron transparency at different angles. Tilt axis is indicated by an orange dashed line. **d**) The width of the lamella is indicated by a white double arrow and the yellow dashed square indicates an approximate area that is accessible at ±60° during tilting along the B-axis

film, which contracts less than gold EM grids at a lower temperature (film crinkling) [20]. The thermal expansion coefficients for cell material (vitreous ice) and substrate (amorphous carbon) were taken from the literature as $\alpha_c = 2 \times 10^{-5} K^{-1}$ [27] and $\alpha_s = 0.79 \times 10^{-5} K^{-1}$ [20], respectively.

We next aimed to compare the von Mises stress between different milling geometries. To this end, three milling geometries were modeled: (i) a rectangular milling geometry with T-joints; (ii) a rectangular geometry with ramp-step joints, formed by progressively narrowing the milling rectangles as the process advances; (iii) a geometry with Y-joints, arising from trapezoidal milling patterns demonstrated above. Stress relief cuts, which were empirically determined to reduce lamella distortions, were included in all milling geometries. For simplicity, all simulations used the thermal expansion coefficient of amorphous carbon substrate, but this choice in general is not essential for the obtained results. Details of the simulation setup can be found in Materials and Methods. The simulated undeformed geometry of the cell milled with rectangular patterns resulting in T-joints or ramp-step joints, along with the displacement field and the resulting deformed geometry, are shown in Fig. 6A-L. The displacement results corresponding to the cell milled with trapezoid milling patterns resulting in Y-joints are shown in Fig. 7A-C. All geometries yielded similar results: a mostly isotropic contraction across the whole body is observed. The displacement field at the lamella was mostly suppressed, given that its norm is 0.001 µm near the centre of the lamella and up to 0.075 µm in the rest of the body. The largest displacements in the lamella were observed in its outermost surface parallel to the xz plane (Figs. 6A, B, G and H and 7A and B), where slight buckling is observed in the z direction. The most obvious difference between the joint geometries is the buckling of the joints in the x direction, which is significant in the T-joint (Fig. 6C), but less noticeable in the ramp-step joint (Fig. 6L) and Y-joint (Fig. 7C). This is due to the increased distance between the lamella and the joints, which prevents buckling. Ramp-step joints, which are commonly used, showed a similar von Mises stress distribution as in a lamella connected with a T-joint.

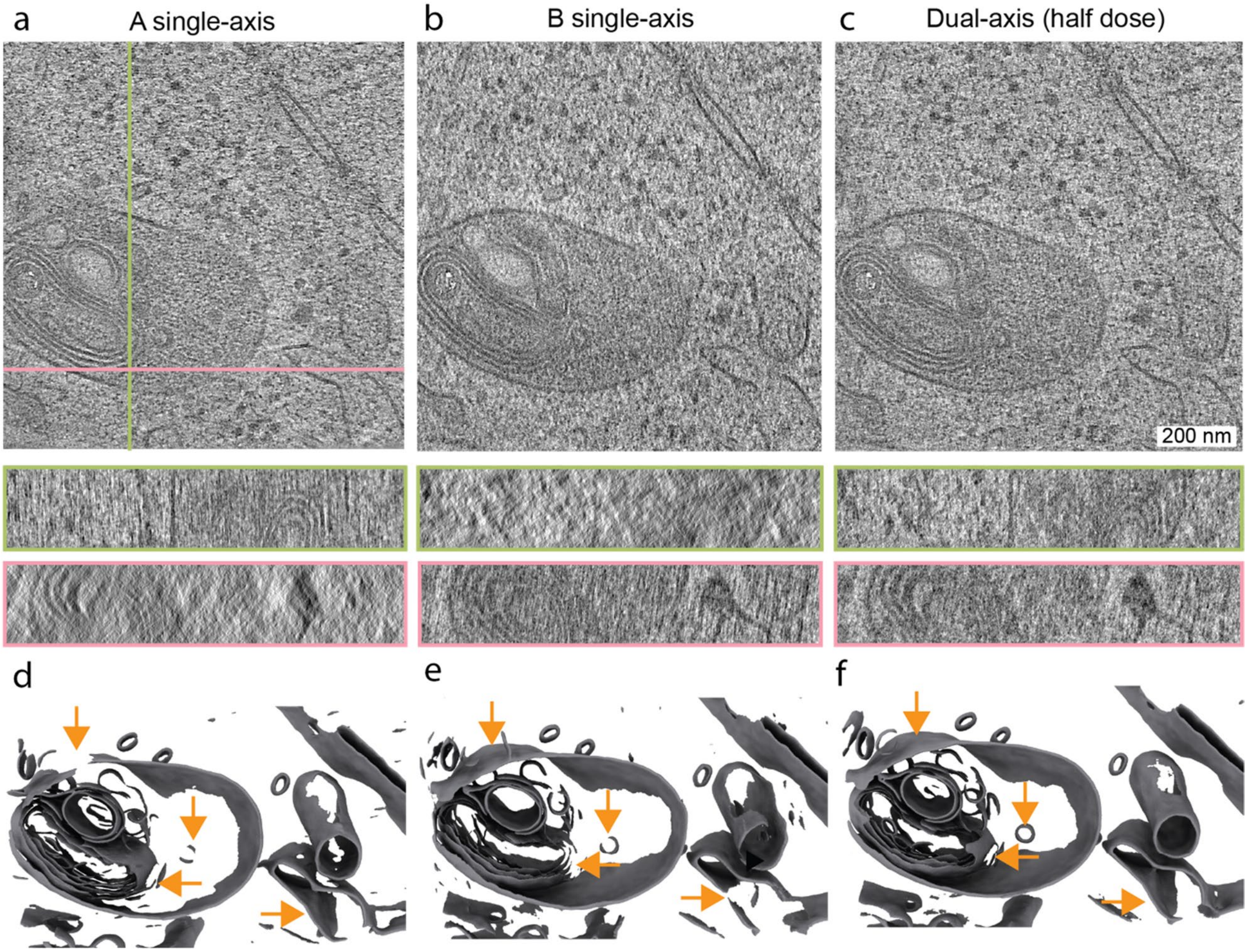

Fig. 4 Single-axis versus dual-axis on-lamella cryo-ET. **a-c**) Orthogonal slices of tomograms reconstructed from single-axis tomograms A and B, and of a dual-axis tomogram. Each single-axis tomogram was reconstructed from a tilt series acquired with a total dose 65 $e^{-}/Å^{2}$. Dual-axis tomogram was reconstructed from tilt series A and B, where even frames were removed from each projection to have a final dose of 65 $e^{-}/Å^{2}$. Green and pink lines indicate orthogonal xz and yz slices, which are shown below in green and pink frames. (**d-f**) MemBrain segmentations are shown below with orange arrows highlighting differences

We quantified the von Mises stress, related to the Frobenius norm of the traceless part of the stress tensor (see Materials and Methods), to identify weak regions prone to fracture within the lamella milled inside a vitrified cell. The von Mises stresses for the T-joints are shown in Fig. 6D-F, whereas the analogous results for the ramp-step joints are shown in Fig. 6J–L and for the Y-joints in Fig. 7D-F. In the T-joint geometry, a build-up of stress at the joint is observed. Such stress concentration is due to the sharp contact angle, which experiences stresses of up to 30 MPa in comparison to 0.1–15 MPa across most of the remaining body. Similarly, regions above and below the lamella with T-joints show high stress due to the buckling of the joints. In contrast, both the ramp-step joint and the Y-joint concentrate stress in the lamella itself, ranging between 20 and 37 MPa. Stress in the joints is notably reduced due to the suppression of the buckling. In all geometries high stress is observed at the bottom surfaces, which represent the interface with the substrate. This is a consequence of an idealised geometry with a sharp contact angle; the real contact angle will be rounded, have a larger surface area and thus lower stress.

The data above showed that increased distance between stress relief cuts and lamella prevents buckling, which concentrates the stress in the lamella volume. We therefore simulated two alternative designs that position the stress relief cuts closer to the lamella: one with triangular cuts and another with V-shaped cuts. The results indicate that both stress relief cuts reduce the von Mises stress in the lamella more than vertical stress relief cuts (Fig. 8A, B). We therefore tested whether triangular and V-shaped stress relief cuts are also feasible in practice and successfully milled three lamellas for each geometry. No lamella was broken during the transfer to the cryo-transmission electron microscope (Fig. 8C-H).

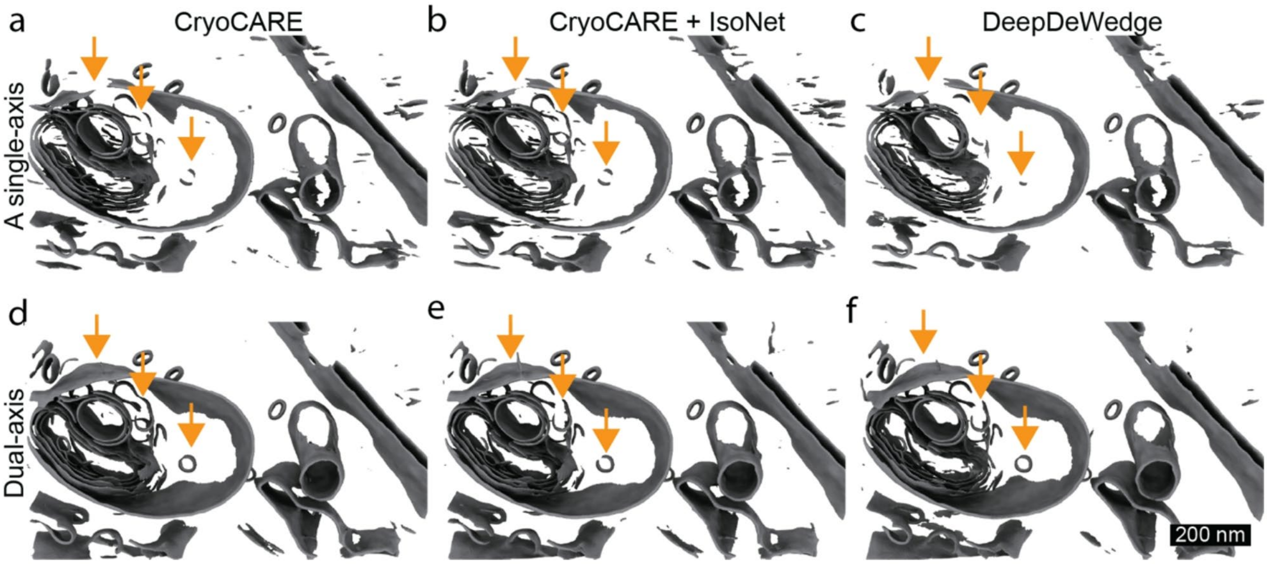

Fig. 5 Comparison of deep learning restoration algorithm and dual-axis tomography. Single-axis (**a-c**) and dual-axis (**d-f**) tomograms denoised with cryoCARE (**a**, **d**), denoised with cryoCARE and missing wedge corrected with IsoNet (**b**, **e**), or denoised and missing wedge corrected with DeepDeWedge (**c**, **f**). Missing wedge corrected dual-axis tomograms were corrected before combination in Etomo. Orange arrows indicate missing information, which is completed in the dual-axis tomogram

Because the elastic equations lead to stress localization at sharp edges, a possible workaround to mitigate the build-up of von Mises stress is to use rounded joints. We explored this alternative by simulating geometries with variable radius of curvature of the joints connecting the lamella to the cell body. Starting with the orthogonal milling pattern, we introduced a curvature ranging up to 1.45 μm and calculated the peak stress. Through the stress distributions in Fig. 9A-C it is shown that having joints with low radius of curvature drastically lowers stress at T-joints. The calculated stress at the curved T-joint has a minimum around a radius of 0.32 μm, as shown in Fig. 9D, beyond which the increase in material appears to play a larger role.

Finally, we simulated a rectangular geometry with a T-joint on one side and a notch on the other side, first applied by Kelley et al. in the waffle milling approach [29]. As expected, releasing lamella on one side mitigates compression and releases stress in the T-joint (Fig. 9E).

Discussion

Cryo-FIB has opened a way to study unperturbed vitrified cellular environments in 3D and molecular resolution. Furthermore, the resolution can be improved by subtomogram averaging. Yet, low-abundant proteins, proteins with intrinsically disordered domains, and proteins with small sizes are often difficult to assess by subtomogram averaging. Hence, the interpretation of a cellular crowded environment often relies on direct analysis of the tomograms. Dual-axis cryo-ET contains additional 3D information and provides a tomogram with reduced resolution anisotropy. This facilitates data interpretation, 3D segmentations, and direct visualization of small protein complexes and filamentous structures that can suffer from information loss depending on their orientation to the tilt axis [11].

Here, we established a cryo-FIB milling trapezoid pattern to prepare cryo-lamellae compatible with dual-axis cryo-ET (Figs. 1 and 2). This approach additionally removes edges of the cell body, thereby enabling dual-axis tomography (Fig. 3) and facilitating tilting, even when the Autogrid is not perfectly loaded into the cassette (Thermo Fisher Scientific microscopes). With PACE tomo [23], the time required for acquiring single- and dual-axis tilt series is no longer a major limiting factor. Our data demonstrate that dividing the electron dose between two orthogonally oriented tilt series enables alignment via patch tracking, followed by reconstruction of two tomograms. We do not observe a statistically significant increase in alignment error caused by the lower electron dose in the micrographs. These volumes can then be combined into a dual-axis tomogram. We utilized unsupervised 3D segmentations using MemBrain [25] to demonstrate that dual-axis cryo-ET provides increased information on organelle structure in 3D, outperforming single-axis cryo-ET (Fig. 4). Additionally, we compared the 3D information of dual-axis tomograms with those generated using deep-learning algorithms for missing wedge restoration in Fourier space, such as IsoNet [7] and DeepDeWedge [10]. Our analysis revealed that deep learning-driven restoration is incomplete and, to some extent, inaccurate (Fig. 5). To address

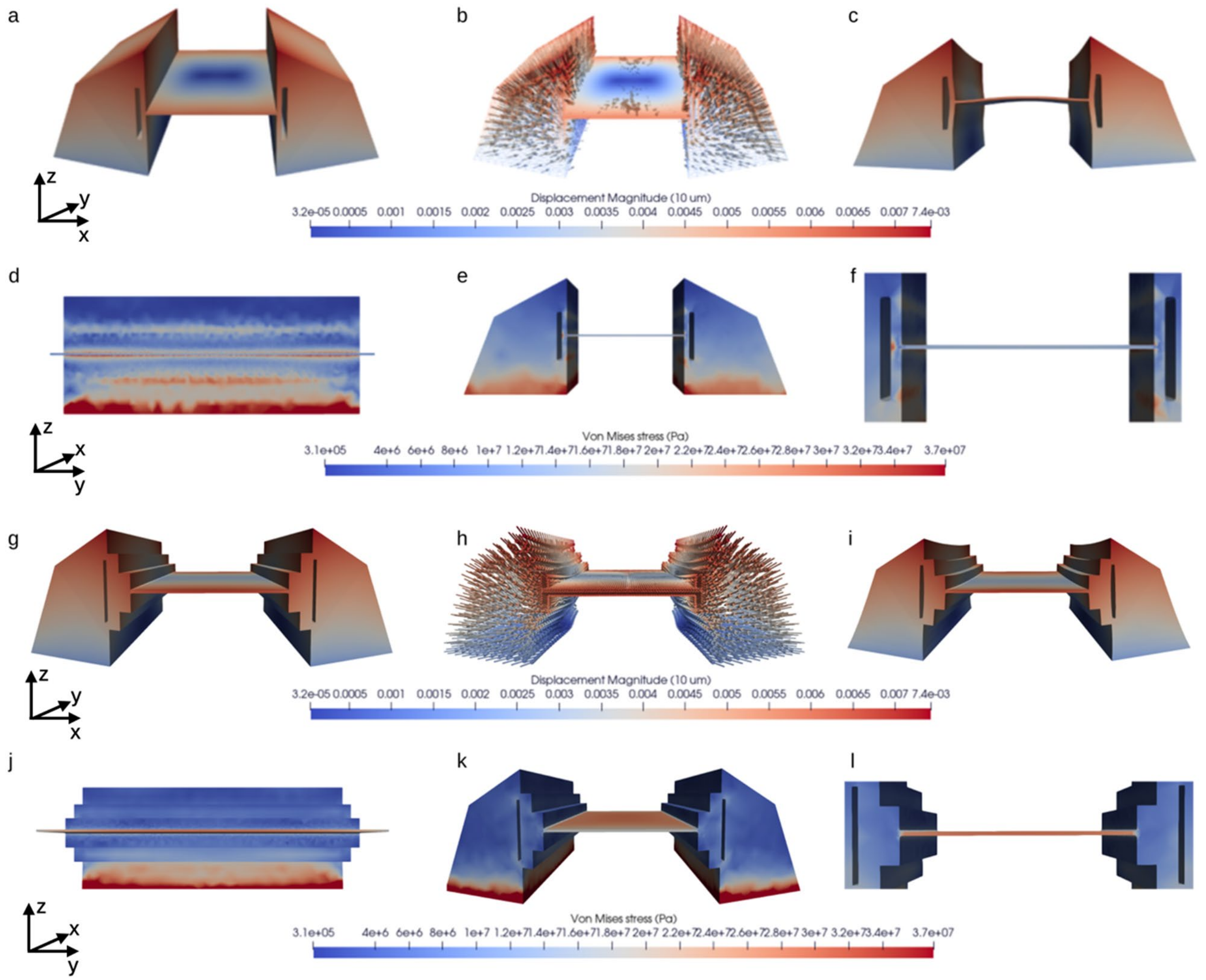

Fig. 6 Finite element simulation of the mechanical response of lamella with T-joints to thermal strain**. a-b**) Displacement field magnitude (**a**) and vector field (**b**) of a simulated geometry with T-joints. **c)** Deformed configuration of the lamella after straining, augmented by a factor of 15 for clarity. **d-f**) Von Mises stress for slices along the center xz plane (**d**) and zy plane (**e**), the latter of which is zoomed in to resolve the field at the lamella (**f**). **g-l**) simulation results for a ramp-step geometry in the same layout as (**a-f**)

this limitation, we propose leveraging dual-axis tomograms as a training dataset to improve the prediction accuracy of deep-learning-based missing wedge restoration methods. The main limitation of dual-axis cryo-ET comes from the accumulated electron dose of the second tilt series. We have previously shown that electron dose can be further decreased when the Volta phase plate is used [14], and hence, on-lamella dual-axis cryo-ET will in the future benefit from laser phase plate implementation, which shows promising results [30, 31]. Future work will need to evaluate the feasibility and benefits of subtomogram averaging in this context. Combining Warp and M refinement across both axes may enhance reconstructions from tilt series acquired over a ± 40–60° range. Currently, however, available subtomogram averaging pipelines do not support merging particles derived from dual-axis tomograms.

Despite automation, cryo-FIB lamella preparation remains a major bottleneck of in situ cryo-ET. Due to lateral pressure which is released during milling lamella can bend or crack. To evaluate the stability of lamellae produced by the rectangular and trapezoid milling patterns, we use theoretical modelling to identify stress points on lamella. The FEM simulations confirmed the protective role of the stress-release cuts against thermal wrinkling for the orthogonal geometry. As shown in Fig. 6A and C, the contraction causes the joints to buckle inwards, which in turn suppresses the in-plane displacement across the lamella at its centre. As a result, the displacement norm across the lamella is almost two orders of magnitude lower compared to that of the rest of the body (Fig. 6A). In contrast, the lamella shows the greatest in-plane displacement along its outer edges parallel to the xz plane, where no joints are present, and even displays

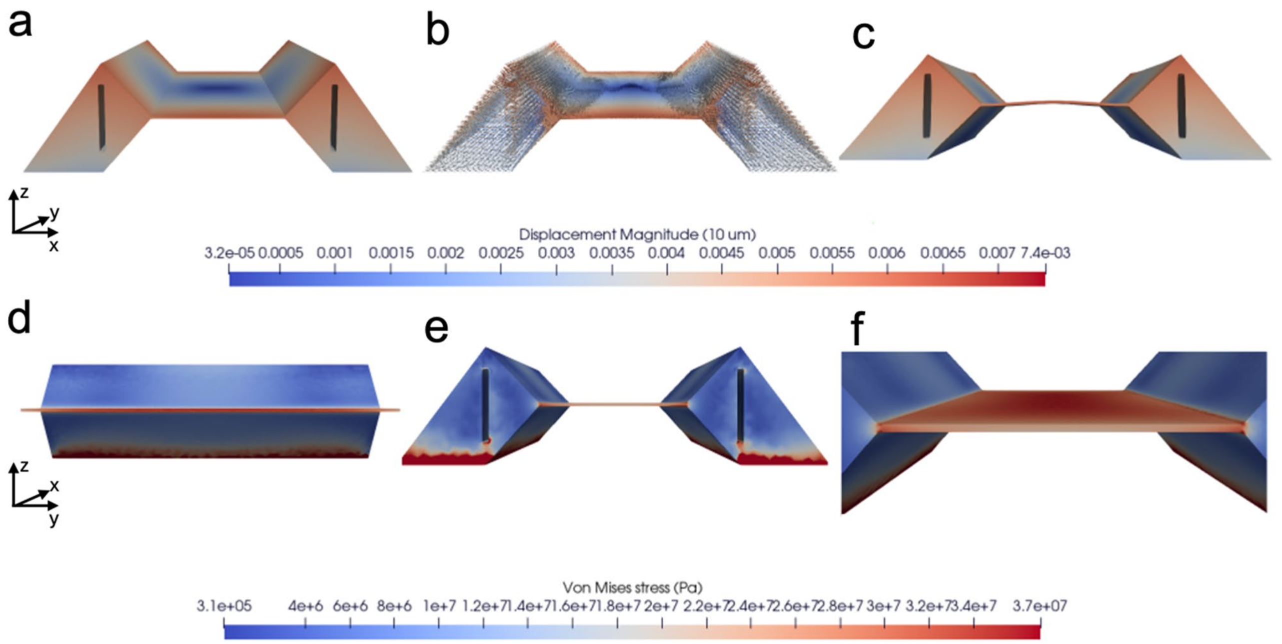

Fig. 7 Finite element simulation of the mechanical response of lamella with Y-joints to thermal strain. **a-b**) Displacement field magnitude (**a**) and vector field (**b**) of a simulated geometry with Y-joints. **c)** Deformed configuration of the lamella after straining, augmented by a factor of 15 for clarity. **d-e**) Von Mises stress for slices through the centre of the lamella along the xz plane (**d**) and zy plane (**e**). **f**) Isotropic view for the von Mises stress results

buckling in the z direction (Fig. 6C). Mechanical protection of the lamella against thermal contraction is paramount, given its fragility stemming from its high aspect ratio. Such fragility is confirmed by the von Mises stress distribution (Fig. 6D, E and F), which exhibits the highest values at the joints (Fig. 6D) due to the thinness of the lamella and the sharp contact angle. Similarly, the buckling of the joints generates further weaker regions above and below the lamella. The region below the lamella is particularly stressed, since it is closer to the substrate that contracts with a different thermal coefficient. We thus identify these regions as the weakest regions that are prone to fracture onset.

Strikingly, the vertical stress relief cuts appear to be less useful in the case of Y-joints (Fig. 7), since the lamella of this geometry experiences a higher von Mises stress than the rest of the body (Fig. 7F). This occurs because the Y-joints and vertical stress relief cuts are far apart. Consequently, their displacement is not affected by the presence of the lamella, as evidenced by the lack of buckling (Fig. 7C), and thus their protective role is reduced compared to the rectangular milling patterns. The simulations thus indicate that the rectangular geometry is not optimal for stress reduction in Y-type junctions. However, our modelling suggests that triangular or V-shaped stress-release cuts should be more effective. We demonstrated that these patterns can be successfully milled to produce lamellae suitable for cryo-TEM imaging (Fig. 8).

Rounding edges at T-joints is an obvious strategy to avoid stress localization at sharp corners and recently has also been suggested by Gorelick et al., where simulations using “fillets” or corner smoothing suggest improving the mechanical stability of lamellae [32]. Our simulations confirmed this prediction, but also showed that keeping too much material leads to detrimental results again.

Figure 9A-C show that the rounding of the joints comes at the expense of an increase in the von Mises stress across the lamella itself: for the smallest radius of curvature (Fig. 9A), the lamella experiences stress of up to 14 MPa, whereas the lamella with largest radius (Fig. 9C) show stress of around 20 MPa. We thus reason that no significant protection is offered if rounding is too strong. Finally, releasing lamella on one side, as used in waffle milling, reduces the thermal stress in the lamella.

Vitreous ice ($\alpha = 2 \times 10^{-5} K^{-1}$) contracts more in response to temperature decrease than the commonly used material for EM grids, in particular amorphous carbon and silicone dioxide (range $\alpha = 0.05 - 1.0 \times 10^{-5} K^{-1}$ depending on details of manufacture). This mismatch generates the high stresses and strains shown in Figs. 6, 7, 8 and 9. Thus, a plausible strategy to minimize thermal stress is to choose a substrate with a similar thermal expansion coefficient to vitreous ice (e.g., Au).

In the future, the theory of inverse problems and rational design can be used to automatically predict new favorable designs. However, the true effect of round edges can only be confirmed experimentally, since the FEM model is highly idealized and does not capture all external factors in the experiment.

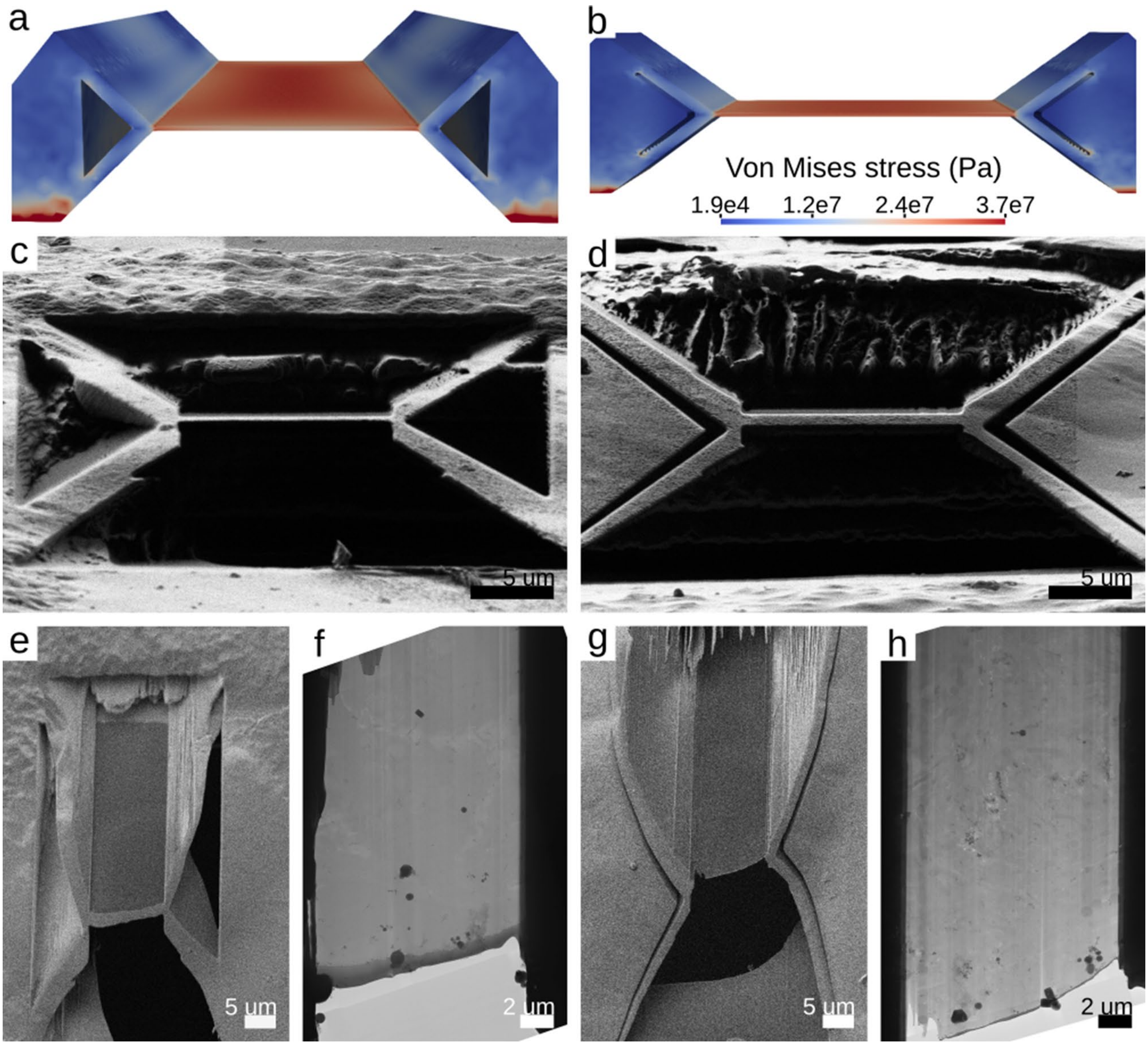

Fig. 8 Triangular and V-shaped stress relief cuts potentially increase lamella stability with Y-joints. (**a**, **b**) Von Mises stress distribution in cells milled with triangular or V-shaped stress relief cuts. (**c**, **d**) representative cryo-FIB images of lamellae milled with triangular (**c**) or V-shaped (**d**) stress-relief cuts. (**e – h**) cryo-SEM images before (**e**, **g**) and cryo-TEM images after (**f**, **h**) transfer to the transmission electron microscope

Conclusions

The cryo-FIB milling approach presented here enables the production of cryo-lamellae compatible with dual-axis cryo-ET. We could show that multi-shot tomography (PACE-tomo) can be applied to facilitate data collection even for dual-axis tomography. Dual-axis tomograms of the cellular environment outperform current missing wedge restoration methods applied to single-axis tomograms. As a result, dual-axis tomograms enhance the interpretability and segmentation accuracy of cryo-preserved cellular structures and can serve as ground truth for deep learning–based missing wedge restoration approaches. This work highlights that further development of mechanically stable dual-axis stages for Krios systems, allowing free rotation, would not only enable dual-axis tomography but also facilitate the rotation of FIB-AutoGrids during stage loading. Developments in stage precision, energy filters, direct electron detectors, and phase plates are likely to further reduce the electron dose required for dual-axis cryo-ET. These advances will make dual-axis tomography an even more powerful tool for accurate and quantitative analyses in structural cell biology.

In addition, the computational model presented here offers a valuable tool for assessing and optimizing lamella shapes produced by novel milling patterns. Exploring

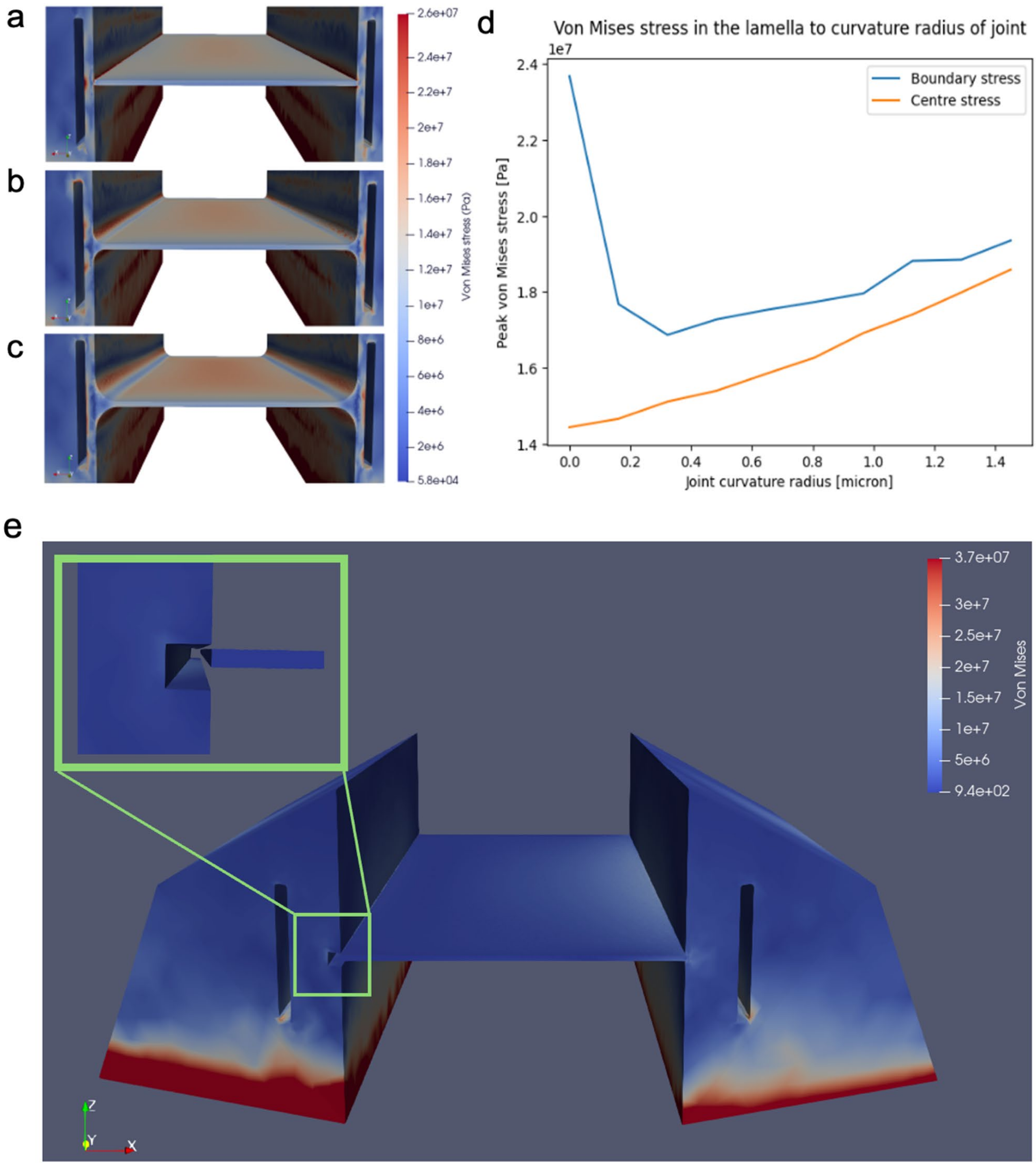

Fig. 9 Calculated average stress at lamella body joint for different curvature radii. **a-c**) Von Mises stress distribution zoomed in to the lamella region of with T-joints with joint curvature radius 0 µm (**a**), 0.32 µm (**b**), and 1.45 µm (**c**). **d**) Peak von Mises stress set out against the curvature radius. **e**) Von Mises stress distribution for lamella with a T-joint on one side and a notch on the other side

different combinations of junction and stress-release cut geometries represents a promising direction for future research. While here this has been done motivated by existing experimental designs, in the future this might be automated using recent advances in automatic differentiation and shape optimization [33].

Abbreviations

Cryo-ET	Cryo–electron tomography
Cryo-FIB	Cryo–focused ion beam

FEM finite element method

Acknowledgements
We thank the Infectious Diseases Imaging Platform (IDIP) at the Center for Integrative Infectious Disease Research Heidelberg and the cryo-EM network at the Heidelberg University (HD-cryoNET) for support and assistance. The authors gratefully acknowledge the data storage service SDS@hd supported by the Ministry of Science, Research, and the Arts Baden-Württemberg (MWK), the German Research Foundation (DFG) through grant INST 35/1314-1 FUGG and INST 35/1503-1 FUGG.

Author contributions
M.W-M. performed data processing and analysis and prepared Figs. 4 and 5.; C.M. and S.G.M. performed modeling of lamellae and prepared Figs. 6, 7 and 8. L.Z. prepared the samples; P.C. and U.S.S. conceptualized the study. P.C. prepared Figs. 1, 2 and 3, performed cryo-FIB and cryo-ET. P.C. and U.S.S. wrote the manuscript and obtained funding. All authors reviewed the manuscript.

Funding
Open Access funding enabled and organized by Projekt DEAL. This work was supported by research grants from the Chica and Heinz Schaller Foundation (Schaller Research Group Leader Programme) and the Deutsche Forschungsgemeinschaft (DFG, German Research Foundation) to P.C. and U.S.S. (project no. SFB1129/3–240245660 – P04 and P19 and – SFB-1638/1–511488495 – P03 and Z03). Moreover, this work was also supported by the DFG under Germany's Excellence Strategy - EXC 2082/1-390761711 (the cluster of excellence 3DMM2O) to U.S.S. P.C. acknowledges the DFG Heisenberg programme (project number 537227910).

Data availability
Tomograms and raw data were deposited into the EMDB and EMPIAR database and can be accessed under an accession code: EMD-56089 and EMPIAR-13168, respectively.

Declarations

Ethics approval and consent to participate
Not applicable.

Consent for publication
Not applicable.

Competing interests
The authors declare no competing interests.

Author details
[1]Department of Infectious Diseases-Virology, Heidelberg University, Heidelberg, Germany
[2]BioQuant-Center for Quantitative Biology, Heidelberg University, Heidelberg, Germany
[3]Institute for Theoretical Physics, Heidelberg University, Heidelberg, Germany

Received: 21 April 2025 / Accepted: 6 January 2026

References

1. Lam V, Villa E. Practical approaches for Cryo-FIB milling and applications for cellular Cryo-Electron tomography. Methods Mol Biol. 2021;2215:49–82.
2. Marko M, Hsieh C, Moberlychan W, Mannella CA, Frank J. Focused ion beam milling of vitreous water: prospects for an alternative to cryo-ultramicrotomy of frozen-hydrated biological samples. J Microsc. 2006;222(Pt 1):42–7.
3. Rigort A, Bauerlein FJ, Villa E, Eibauer M, Laugks T, Baumeister W, Plitzko JM. Focused ion beam micromachining of eukaryotic cells for cryoelectron tomography. Proc Natl Acad Sci U S A. 2012;109(12):4449–54.
4. Schaffer M, Engel BD, Laugks T, Mahamid J, Plitzko JM, Baumeister W. Cryo-focused ion beam sample Preparation for imaging vitreous cells by Cryo-electron tomography. Bio Protoc. 2015;5(17).
5. Kudryashev M. Resolution in electron tomography. In: Hanssen E, editor. Cellular Imaging: Electron Tomography and Related Techniques. Cham: Springer International Publishing; 2018. p. 261–282.
6. Palmer CM, Lowe J. A cylindrical specimen holder for electron cryo-tomography. Ultramicroscopy. 2014;137(100):20–9.
7. Liu YT, Zhang H, Wang H, Tao CL, Bi GQ, Zhou ZH. Isotropic reconstruction for electron tomography with deep learning. Nat Commun. 2022;13(1):6482.
8. Majtner T, Kreysing JP, Tuijtel MW, Cruz-León S, Liu J, Hummer G, Beck M, Turoňová B. CryoTIGER: Deep-learning based tilt interpolation generator for enhanced reconstruction in cryo electron tomography. bioRxiv. 2024;2024.12.17.628939.
9. Moebel E, Kervrann C. A Monte Carlo framework for missing wedge restoration and noise removal in cryo-electron tomography. J Struct Biol X. 2020;4:100013.
10. Wiedemann S, Heckel R. A deep learning method for simultaneous denoising and missing wedge reconstruction in cryogenic electron tomography. Nat Commun. 2024;15(1):8255.
11. Mastronarde DN. Dual-axis tomography: an approach with alignment methods that preserve resolution. J Struct Biol. 1997;120(3):343–52.
12. Rachel R, Walther P, Maassen C, Daberkow I, Matsuoka M, Witzgall R. Dual-axis STEM tomography at 200 kV: Setup, performance, limitations. J Struct Biol. 2020;211(3):107551.
13. Sousa AA, Azari AA, Zhang G, Leapman RD. Dual-axis electron tomography of biological specimens: extending the limits of specimen thickness with bright-field STEM imaging. J Struct Biol. 2011;174(1):107–14.
14. Winter SL, Chlanda P. Dual-axis Volta phase plate cryo-electron tomography of Ebola virus-like particles reveals actin-VP40 interactions. J Struct Biol. 2021;213(2):107742.
15. Chreifi G, Chen S, Metskas LA, Kaplan M, Jensen GJ. Rapid tilt-series acquisition for electron cryotomography. J Struct Biol. 2019;205(2):163–9.
16. Eisenstein F, Danev R, Pilhofer M. Improved applicability and robustness of fast cryo-electron tomography data acquisition. J Struct Biol. 2019;208(2):107–14.
17. Hagen WJH, Wan W, Briggs JAG. Implementation of a cryo-electron tomography tilt-scheme optimized for high resolution subtomogram averaging. J Struct Biol. 2017;197(2):191–8.
18. Buckley G, Gervinskas G, Taveneau C, Venugopal H, Whisstock JC, de Marco A. Automated cryo-lamella Preparation for high-throughput in-situ structural biology. J Struct Biol. 2020;210(2):107488.
19. Klumpe S, Fung HK, Goetz SK, Zagoriy I, Hampoelz B, Zhang X, Erdmann PS, Baumbach J, Muller CW, Beck M, et al. A modular platform for automated cryo-FIB workflows. Elife 2021:10.
20. Booy FP, Pawley JB. Cryo-crinkling: what happens to carbon films on copper grids at low temperature. Ultramicroscopy. 1993;48(3):273–80.
21. Wolff G, Limpens R, Zheng S, Snijder EJ, Agard DA, Koster AJ, Barcena M. Mind the gap: Micro-expansion joints drastically decrease the bending of FIB-milled cryo-lamellae. J Struct Biol. 2019;208(3):107389.
22. Mastronarde DN. Automated electron microscope tomography using robust prediction of specimen movements. J Struct Biol. 2005;152(1):36–51.
23. Eisenstein F, Yanagisawa H, Kashihara H, Kikkawa M, Tsukita S, Danev R. Parallel cryo electron tomography on in situ lamellae. Nat Methods. 2023;20(1):131–8.
24. Kremer JR, Mastronarde DN, McIntosh JR. Computer visualization of three-dimensional image data using IMOD. J Struct Biol. 1996;116(1):71–6.
25. Lamm L, Righetto RD, Wietrzynski W, Poge M, Martinez-Sanchez A, Peng T, Engel BD. MemBrain: A deep learning-aided pipeline for detection of membrane proteins in Cryo-electron tomograms. Comput Methods Programs Biomed. 2022;224:106990.
26. Choi H, Firlar E, Penzes JJ, Mann AB, Kaelber JT. Direct measurement of mechanical properties of vitreous ice by Cryo-FIB. Microsc Microanal. 2023;29(Supplement1):1008–9.
27. Hessinger J, Pohl RO. Annealing of amorphous ice films. J Non-cryst Solids. 1996;208(1):151–61.
28. Landau LD, Pitaevskii LP, Lifshitz EM, Kosevich AM. Theory of Elasticity, 3rd edn. 1986.
29. Kelley K, Raczkowski AM, Klykov O, Jaroenlak P, Bobe D, Kopylov M, Eng ET, Bhabha G, Potter CS, Carragher B, et al. Waffle method: A general and flexible approach for improving throughput in FIB-milling. Nat Commun. 2022;13(1):1857.
30. Du DX, Fitzpatrick AWP. Design of an ultrafast pulsed ponderomotive phase plate for cryo-electron tomography. Cell Rep Methods. 2023;3(1):100387.

31. Remis J, Petrov PN, Zhang JT, Axelrod JJ, Cheng H, Sandhaus S, Mueller H, Glaeser RM. Cryo-EM phase-plate images reveal unexpected levels of apparent specimen damage. J Struct Biol. 2024;216(4):108150.
32. Gorelick S, Velamoor S, Cleeve P, Trepout S, Ying L, Naranbhai V, Ramm G. Mind the corner: fillets in cryo-FIB lamella Preparation to minimise sample loss caused by stress concentration and lamella breakage. J Struct Biol. 2025;217(4):108249.
33. Ham DA, Mitchell L, Paganini A, Wechsung F. Automated shape differentiation in the unified form Language. Struct Multidisciplinary Optim. 2019;60(5):1813–20.

Publisher's note